

Thermodynamic Evaluation and Chemical Vapor Transport of Few-Layer WTe₂

Felix Hansen,*[#] Martin Wels,[#] Samuel Froeschke, Alexey Popov, Daniel Wolf, Bernd Büchner, Peer Schmidt, and Silke Hampel



Cite This: <https://dx.doi.org/10.1021/acs.cgd.0c01004>



Read Online

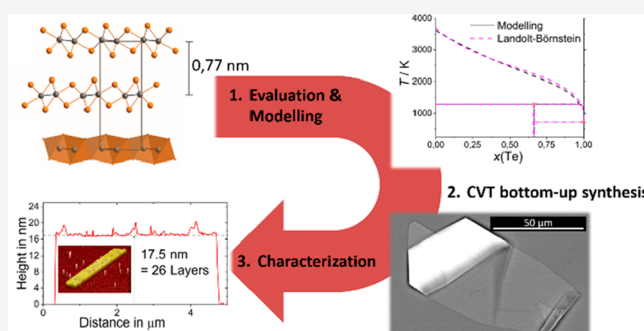
ACCESS |

Metrics & More

Article Recommendations

Supporting Information

ABSTRACT: Tungsten telluride WTe₂ is the sole candidate of a group of two-dimensional layered transition metal dichalcogenides (TMDCs) MX₂ with a thermodynamically stable 1T'-structure at room temperature. The binary system W/Te was audited with respect to a rational approach of planning and realization of a bottom-up synthesis of WTe₂ nanostructures. Thus, the parameters of the synthesis via chemical vapor transports (CVT) were derived by thermodynamic simulations of the reaction pathway according to the Calphad method. Reflecting on the peritectic melting behavior at 1020 °C, the values of $\Delta_f H_m^\circ(298\text{ K}) = -26.5\text{ kJ}\cdot\text{mol}^{-1}$ and $S_m^\circ(298\text{ K}) = 132\text{ J}\cdot\text{mol}^{-1}\cdot\text{K}^{-1}$ have been obtained. According to modeling, crystal growth by short time vapor transport is reasonable under the addition of bromine or TeBr₄ in the temperature range between 650 and 750 °C. Experimental implementation of crystal growth of WTe₂ nanosheets succeeded in a temperature gradient from 725 to 675 °C on yttria-stabilized zirconia (YSZ) (111) substrates, observing the deposition of single crystal sheets of high crystallinity with thicknesses of 15–20 nm (~20–30 layers). The high crystallinity, pristine morphology, and overall quality of the deposited nanosheets is shown by means of atomic resolution transmission electron microscopy, selected area electron diffraction (SAED), and atomic force microscopy as well as profound double-polarized Raman spectroscopy.



INTRODUCTION

Ever since the discovery of free-standing graphene in 2004, two-dimensional (2D) materials reaching from element allotropes to layered compounds have grown widely in research interest.^{1,2} Transition metal-dichalcogenides (TMDCs) MX₂ (M = Mo, W; X = S, Se, Te) are a major group of these layered compounds, and a lot of research has been done on MoS₂, MoSe₂, WS₂, and WSe₂.^{3–5} However, WTe₂ is the only TMDC with a thermodynamically stable 1T'-structure at room temperature, and for this reason alone is of high interest, but yet fewer studies on its mono- and few-layer structures have been performed.

Unlike most TMDCs, 1T'-WTe₂ shows semimetallic behavior since its valence and conduction bands overlap in a small portion.^{6,7} Also it shows superconductive properties at high pressure below 2.8 K and a giant magnetoresistive effect at around 0.53 K.^{8,9} Its topological properties, electrodynamic effects, and various other physical properties make it a fascinating candidate for further research on few-layer materials.^{10–16}

In the stable 1T'-structure of WTe₂, the tungsten atoms are coordinated by distorted octahedra formed of tellurium. Tungsten atoms lie out of the center of the octahedra leading to the buckled structure, and the tellurium atoms are not

evenly distributed within one structural layer of the material but rather form a “wave” shape. The atomic distances change significantly leading to tungsten atoms forming additional bonds between each other shaping “zigzag” chains along the y-axis¹⁷ shown in Figure 1.

In order to further research few-layer WTe₂ by means of, e.g., electronic transport studies, high quality samples are needed without mechanical defects, with high crystallinity and high purity. The most common way to acquire 2D samples is the top-down approach of mechanically exfoliating bulk samples.¹⁸ While this allows us to reach few-layer samples of the material, it also leads to mechanical defects at the edges of the exfoliated crystal, usually rather little lateral dimensions and the exfoliation itself is very time-consuming. Several different experimental approaches to tackle this challenge have been described, such as a variety of chemical vapor deposition (CVD) or atomic layer deposition (ALD) processes with W

Received: July 21, 2020

Revised: September 25, 2020

Published: September 25, 2020

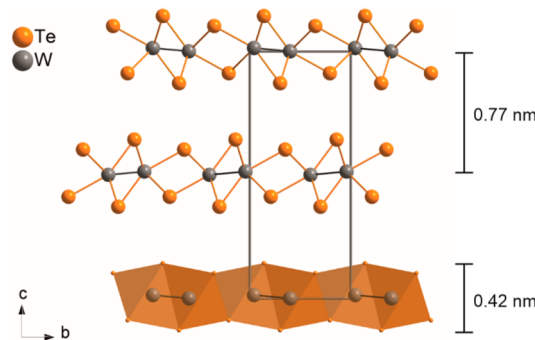


Figure 1. 1T' layered structure of WTe_2 ; linkage of tungsten atoms leads to a distortion of tellurium octahedra. The height of a single layer amounts to 0.42 nm, and the distance of two adjacent layers to 0.77 nm.

films, WCl_6 , and mixed W precursor materials.^{19–24} These methods are mostly focused on the possibility of easy upscaling of the process.

In this work, we present a method of synthesizing few-layer WTe_2 structures on the surface of substrates by means of a chemical vapor transport (CVT) in a closed silica ampule that has proven successful for other 2D materials.^{25,26} Tungsten and tellurium as pure elements as well as a tellurium halide as precursor for the transport agent are the starting materials. This method is ideal for small sample counts of excellent quality down to a few layers.

The goal of this work was to synthesize WTe_2 nanostructures (flat platelets) with lateral dimensions of several microns by a rational approach simulated beforehand, while remaining below 20 nm in height. Yttria-stabilized zirconia (YSZ) was chosen as a substrate due to its high chemical stability at the given reaction conditions, its commercial availability, as well as the low lattice mismatch of its (111) plane with the (001) plane of 1T'- WTe_2 .

The highly crystalline, pristinely shaped few-layer WTe_2 structures on YSZ (111) surfaces were characterized by scanning and transmission electron microscopy (SEM, TEM) and energy dispersive X-ray spectroscopy (EDX). Atomic force microscopy (AFM) was used to determine the height of the WTe_2 crystals, and detailed polarized Raman spectroscopy was used for further investigation of the nanostructure.

EXPERIMENTAL SECTION

Thermodynamic Modeling. Prior to synthesis, CalPhaD modeling of phase diagrams and crystal growth behavior was realized by using the FactSage²⁹ and TRAGMIN²⁸ program packages. Initially, the binary phase diagram (x-T-diagram) of the system W–Te was fitted by using the phase diagram module within the program FactSage. Standard data of the elements were chosen and applied from the implemented databases (FactPS, SGPS). The respective data of the binary compound WTe_2 were collected from the literature.^{29–31} As the heat capacity of WTe_2 was given only for a small temperature

range, extrapolation for the elevated temperature range was realized by using the C_p -function of MoTe_2 .²⁷ An iterative optimization of standard data within the system W/Te succeeded by fitting both the thermal effects of the experimental phase diagram³² and the temperature dependent vapor pressure behavior.²⁹ Finally, optimized values for WTe_2 were obtained according to Table 1.

Rational screening of vapor transport behavior was performed using the program TRAGMIN.²⁸ On the basis of the afore optimized data of WTe_2 the heterogeneous equilibria with bromine as a transport addition were calculated. As a result, the composition of the gas phase, the solubility of all components in the gas phase, the transport efficiencies of identified gaseous species (transport agent and transport efficient gas species), and the transport rate of the deposited solid were obtained. To conclude the simulation results, we derived the dominant vapor transport mechanism. As a special feature of the modeling, we considered the influence of oxygen and water on the gas phase transport of WTe_2 nanoplates and simulated the deposition conditions close to experimental conditions.

Synthesis. All chemicals were purchased from Alfa Aesar (USA) with purities >99.9%. Tungsten powder was reduced in a hydrogen stream for 24 h before using it to reduce surface oxidation and then stored in a glovebox under Argon atmosphere. All preparation steps before sealing the ampule were performed in a glovebox (M. BRAUN, Germany) at <1 ppm of O_2 and <1 ppm of H_2O . Tungsten and tellurium were used in stoichiometric amounts (total of 3–7 mg per experiment). TeBr_4 was used to introduce around 5 atom % bromine into the system, and the rest of the tellurium (up to the stoichiometric amount) was added as pure element. The complete elemental composition was 1:2:0.16 (W/Te/Br). The materials were thoroughly ground together and filled in two-chamber silica ampules (Figure 2) of 1 cm in diameter and 11 cm length. The yttria-stabilized zirconia substrates (CRYSTALTECH GmbH, 3 × 5 mm²) were placed in the ampules, which were then closed permanently by sealing them at $\sim 3 \times 10^{-3}$ mbar inner pressure.

The closed silica ampules were then heated in a two-zone furnace to a temperature gradient between 650 and 750 °C. Before the actual crystal growth, a reverse temperature was applied for 2 h. During this time, the sink was held at the final temperature T_1 , while the source was heated to $T_1 - \Delta T$ for the individual experiment. This way, the starting mixture homogenized to a sufficient amount, and tellurium, which was deposited at the sink area during the sealing of the ampule, was transported back to the source zone. Afterward, the temperature gradient was set for vapor transport to be between 650 °C (min. T_1) and 750 °C (max. T_2).

We varied the temperature gradient from 10 K ($T_2 = 705$ °C, $T_1 = 695$ °C), 50 K ($T_2 = 725$ °C, $T_1 = 675$ °C), up to 100 K ($T_2 = 750$ °C, $T_1 = 650$ °C) as well as the time that the ampules were held at the temperature gradient ($t = 0$ min to 24 h) during the optimization process.

Identification and Characterization. After the reaction, the ampules were quenched to room temperature starting from the source side to avoid further deposition or condensation of the transport agent on the substrate and opened in the glovebox. Samples were analyzed using a “FEI Nova NanoSEM” (FEI, Japan) scanning electron microscope (back scattering electron detector; 30 kV) with an attached “AMETEK Quanta 200/400” (AMETEK, USA) EDX (30 kV) unit with “EDXGenesis” software for quantification, an “icon Dimension” atomic force microscope (AFM) in tapping mode (Si single crystal tips), as well as a “T64000 spectrometer” (Horiba Jobin

Table 1. Optimized Data $\Delta_f H_m^\circ$, S_m° , $C_{p,m}$ of WTe_2

$\Delta_f H_m^\circ(298 \text{ K})$	$-26.5 \text{ kJ}\cdot\text{mol}^{-1}$ $C_{p,m}(T_0..T_1) = \sum (a_i \cdot T^i) \text{ J}\cdot\text{K}^{-1}\cdot\text{mol}^{-1}$	$S_m^\circ(298 \text{ K})$	$132.7 \text{ J}\cdot\text{K}^{-1}\cdot\text{mol}^{-1}$
$T_0..T_1/\text{K}$	$a_0(T^0)$	$a_1(T^1)$	$a_2(T^{-2})$
1...145 ³⁰	-5.869	0.334534	305.7171
145...298 ³⁰	24.089	-4.265×10^{-2}	-4.195×10^4
298...1501 ²⁷	20.1881	2.578×10^{-4}	-1.689×10^5
			$a_3(T^2)$
			0.0

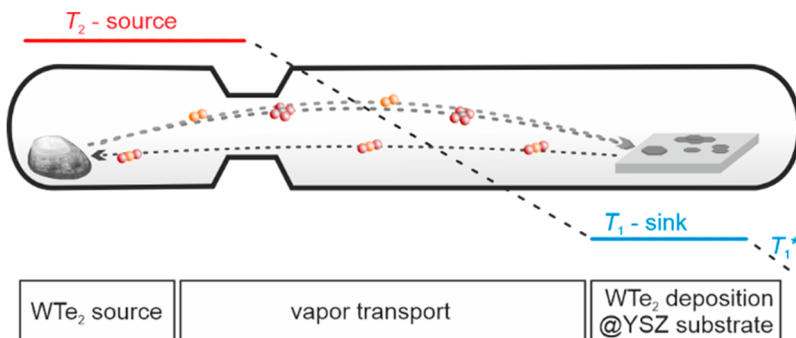


Figure 2. Setup of the CVT process in a closed two-chamber ampule with the starting material on the source and the substrate on the sink side. Addition of bromine achieves formation of the transport relevant gas species, as WBr_4 and Te_2 . A change in the equilibrium state within the temperature gradient ($T_2 > T_1$) causes the volatile species to diffuse to the sink side, and WTe_2 is deposited with a reversal of the equilibrium. T_1^* is the point of the lowest temperature in the tip of the sink of the ampule with a second, small temperature gradient from the substrate positioned at T_1 .

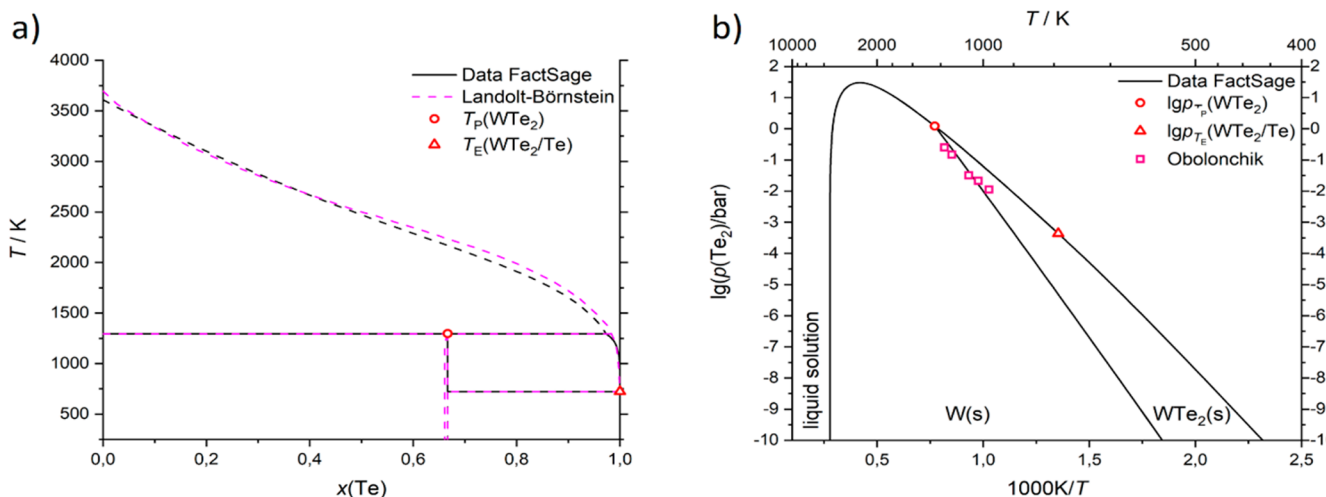


Figure 3. (a) Phase diagram of binary system W/Te, calculated by using FactSage,²⁷ in comparison to experimental data; (b) phase barogram depicting the temperature-dependent vapor pressure behavior, calculated by using FactSage, in comparison with experimental data.²⁹ The characteristic points of phase diagram are marked as \circ peritectic temperature $T_p(\text{WTe}_2)$ and Δ eutectic temperature $T_E(\text{WTe}_2/\text{Te})$.

Yvon, USA) for the polarized Raman spectroscopy. The laser used in the Raman device was a linear polarized “Torus Laser” ($\lambda = 532 \text{ nm}$, $P = 3 \text{ mW}$, $A_{\text{spot}} = 0.8 \mu\text{m}^2$) that was turned in 15° steps for a full 360° during the measurement. Bright field and high-resolution TEM imaging as well SAED measurements were conducted at a Titan3 80–300 instrument (Thermo Fisher Company, USA). The images were acquired using an acceleration voltage of 300 keV. For atomic resolution imaging, we employed an aberration corrector providing a resolution of up to 0.08 nm.

RESULTS AND DISCUSSION

Rational Synthesis Planning by Modeling of the CVT Process.

Prior to experimental synthesis efforts, thermodynamic assessment of the system was realized, and thus rational synthesis planning by modeling of the process became possible. Initially, standard data of WTe_2 were proven on consistency and optimized by modeling the phase diagram and barogram. Completely fitting the experimental results, the phase diagram reveals peritectic behavior of WTe_2 as the sole binary phase of the system. Peritectic temperature is calculated to be 1020°C ; composition thereby considerably shifts toward a tellurium-rich melt with about 97% Te (Figure 3a). The melting behavior of WTe_2 is additionally complicated by high vapor pressure of the tellurium-rich melt, reaching above 1.2

bar at the peritectic point. As standard methods of thermal analysis are not suited to investigate the further course of the liquidus line under given pressure conditions, the experimental liquidus line is dashed in Figure 3a. Calculation of the concerning phase barogram proves this finding (Figure 3b). With a composition of about 57% Te, a maximum pressure of the melt of 30 bar (at 2060°C) is obtained by computation. However, the vapor pressure behavior of solid WTe_2 is of more interest for rational synthesis approaches: In accordance with experimental data,²⁹ the phase barogram is computed showing WTe_2 decomposes mainly by equilibrium 1.



Suitable conditions for phase pure synthesis of WTe_2 can be deduced under the consideration that optimum synthesis conditions prevail at a temperature with a corresponding vapor pressure $p(\text{Te}_2)$ of about 10^{-3} to 10^{-1} bar.^{33–35} Thus, appropriate synthesis temperatures reach from 620 to 850°C (Figure 3b). Higher temperatures must be avoided, as the decomposition reaction proceeds with a significant amount of tellurium in the gas phase and the formation of metallic tungsten, resulting in non-phase-pure source solids.

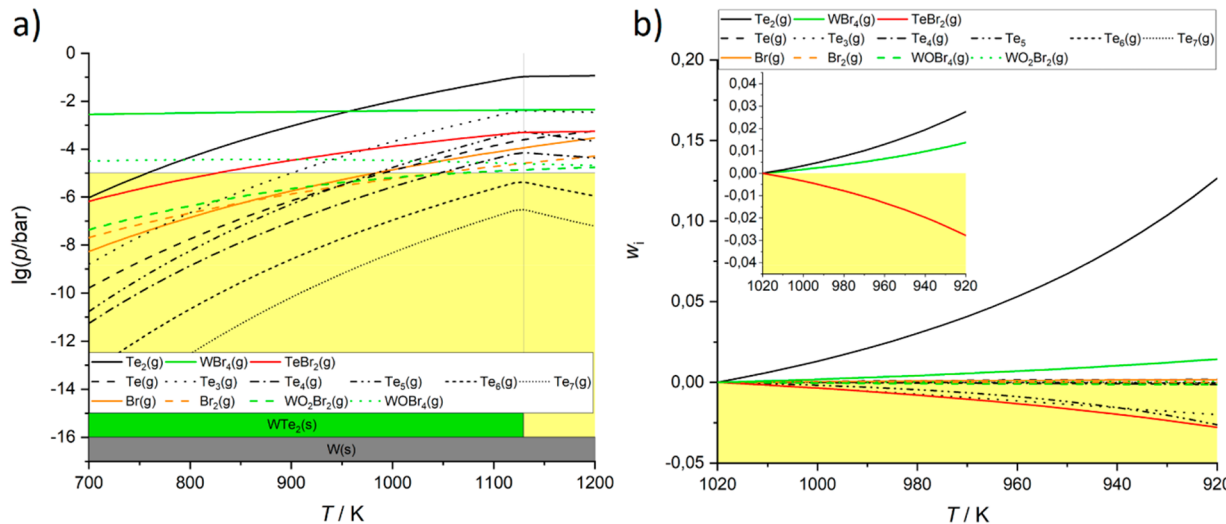


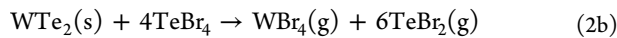
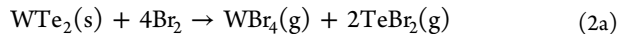
Figure 4. (a) Composition of the gas phase above the source solid WTe_2 under the addition of bromine, calculated by using FactSage;²⁷ (b) efficiency of gas species for the vapor transport reaction of WTe_2 in a temperature gradient from $T_2 = 1100$ K, calculated by using TRAGMIN;²⁸ species with $w_i < 0$ are depleted at the source temperature (T_2) and released in the sink (T_1); thus TeBr_2 functions as a transport agent, while otherwise species with $w_i > 0$ are formed at T_2 . Thus, mainly WBr_4 and Te_2 are responsible for the migration.

While tungsten itself is not volatile under decomposition according to eq 1, addition of halides can provide the formation of tungsten-containing gas species. Thus, chemical vapor transport (CVT)^{36–38} comes into focus for crystal growth of WTe_2 . Crystallization of WTe_2 by chemical vapor transport is first reported by Brixner and Brown with the aim of crystal structure determination.^{17,39} The use of bromine as a transport additive is mentioned, but otherwise no further experimental details are given. Recently, growth of bulk crystals of WTe_2 by vapor transport is described by using Br_2 in the gradient from 750 to 650 °C.^{10,13}

Aspiring a rational approach for planning of crystal growth by vapor transport, sophisticated thermodynamic evaluation has been realized for the pertinent system $\text{W}/\text{Te}/\text{Br}$. On the basis of the afore optimized thermodynamic standard data of WTe_2 , calculations were carried out to analyze the composition of the gas phase as well as the flux of individual species within a temperature gradient.²⁸ Thus, the formation of dominant gaseous species can be identified, and the mechanism of vapor transport can be deduced.

According to the simulation of heterogeneous phase equilibria, addition of bromine mainly causes formation of bromine-containing species of both tungsten and tellurium (chiefly $\text{WBr}_4(\text{g})$ and $\text{TeBr}_2(\text{g})$) in the first reaction 2a. However, the addition of TeBr_4 as a brominating agent causes formation of the same species (2b), while it is easier to handle and is therefore preferable. Different tellurium species are formed in the course of additional homogeneous gas phase equilibria 3.

Heterogeneous reaction:



Homogeneous gas phase equilibria:

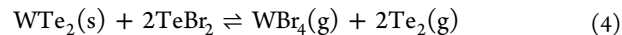


With the presence of oxygen or water, moreover, the formation of tungsten oxide bromides ($\text{WO}_2\text{Br}_2(\text{g})$ and $\text{WOBr}_4(\text{g})$) is

observed. Nevertheless, their partial pressure remains low and does not influence the transport behavior. Partial pressures of bromine species $\text{Br}_2(\text{g})$ and $\text{Br}(\text{g})$ drop behind, thus reflecting that bromine should not be the transport agent (Figure 4a). Sharing the range of partial pressure of transport-relevant species, that have to be at least 10^{-4} – 10^{-5} bar,^{26,40} WBr_4 , TeBr_2 , and Te_2 finally become important for dissolution and migration of WTe_2 in the temperature range from 550 to 850 °C.

Emphasizing the transport efficiencies, $\text{TeBr}_2(\text{g})$ is found to act as the transport agent. The negative slope of calculated transport efficiency w_i indicates the function of the transport agent: this gas species is depleted at the source and released at the sink (see Figure 4b). On the other hand, transport-relevant species reveal positive values w_i , since they evaporate at the source and condense at the sink to form the crystalline solid; see equilibrium 4. The transport according to the dominant equilibrium 4 then proceeds as an endothermic reaction, i.e., from T_2 to T_1 ($T_2 > T_1$). Furthermore, some gas species appear to have an efficiency with values of w_i not equal to zero. In fact, these values result from homogeneous equilibria 3 and do not participate in the mass flow.

Chemical vapor transport:



Finally, suitable conditions for the formation of nanocrystals in deposition experiments can be deduced from modeling: For phase pure precipitation of WTe_2 , the gradient between source and sink must be less than or equal to 100 K. Otherwise, condensation of tellurium would occur, as the equilibrium pressure line of the condensed tellurium would then be cut (see Figure 3b). With this respect, modeling shows sufficient dissolution of WTe_2 by equilibrium 4 at $T_2 = 750$ °C and phase pure crystallization at T_1 not lower than 650 °C.

As an additional indicator for optimum conditions for the formation of nanocrystals in short-term deposition experiments, a transport rate of less than 1 mg h⁻¹ is aspired.^{26,40} Again, the gradient $T_2 = 750$ °C to $T_1 = 650$ °C appears to be

well suited for the intended synthesis approach, which is in agreement with recent experiments on bulk materials.^{10,13}

On the basis of these findings, the following experiments on the crystal growth of few layered WTe₂ could be rationally designed and successfully realized.

Experimental: Temperature Gradient and Reaction Time. After setting the basic conditions of the synthesis approach by rational planning, an optimization process was performed to find the perfect combination of temperature gradient and reaction time for the synthesis of WTe₂ nanosheets. For this purpose, the mean temperature between T_2 and T_1 was appointed to 700 °C.

The optimization of the temperature gradient leads to a significant change in the nucleation rate and shape of the crystals grown on the substrate (Figure 4).

A gradient of $\Delta T = 10$ K (Figure 5a) leads to almost no visible growth of WTe₂ structures, whereas we find tellurium

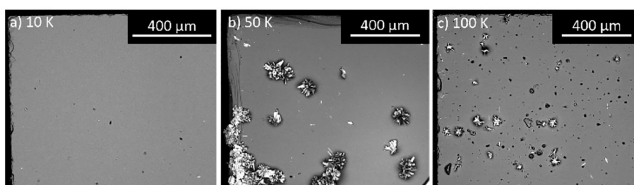


Figure 5. SEM image comparison of WTe₂ microstructures grown on YSZ (111) at different temperature gradients. $T_0 = 700$ °C, $t = 12$ h. (a) $T_2 = 705$ °C, $T_1 = 695$ °C; almost no growth of WTe₂, (b) $T_2 = 725$ °C, $T_1 = 675$ °C; several crystals and agglomerates, moderate nucleation rate, (c) $T_2 = 750$ °C, $T_1 = 650$ °C ; high nucleation rate, small crystals, irregularly shaped.

crystals deposited on the substrate in several cases. At $\Delta T = 50$ K (Figure 5b), the nucleation rate reaches its optimum with regularly shaped crystals in several agglomerates, whereas at $\Delta T = 100$ K (Figure 5c) the nucleation rate seemed to rise too high, and we got irregularly shaped, elongated, “rod-like” crystals.

To reach optimum conditions for the growth of nanosheets, we also varied the reaction time from 0 min (heating up and quenching instantly after), up to 24 h.

After a short time (30 min), nuclei start to form on the substrate and increase in size and number during the next hours (Figure 6b,c). However, no nanosheets can be found on the substrate after these reaction times. Regularly shaped microstructures are found after 10–14 h on the surface of the substrate between the bigger crystal agglomerates (Figure 6d). After 24 h, no smaller structures are visible, and only the bigger WTe₂ agglomerates remain on the substrate (Figure 6e).

This effect might be caused by a second transport happening in parallel in the ampule after a period of time. Since the substrate can never be at the very end of the ampule due to geometrical limitations, there is a second, much lower temperature gradient present between the innermost point of the substrate and the coldest point of the ampule in the sink tip. According to the temperature profile of the used furnace, this gradient between T_1 and T_1^* (see Figure 2) is around 7 K at $\Delta T = 50$ K. After longer reaction times, this leads to the smaller sized crystals dissolving into the gas phase and to the growth of bigger crystals on the wall of the ampule at T_1^* rather than an Ostwald-ripening process on the substrate surface. Because of the higher gradient from T_1 to T_1^* , this effect is stronger for higher values of ΔT .

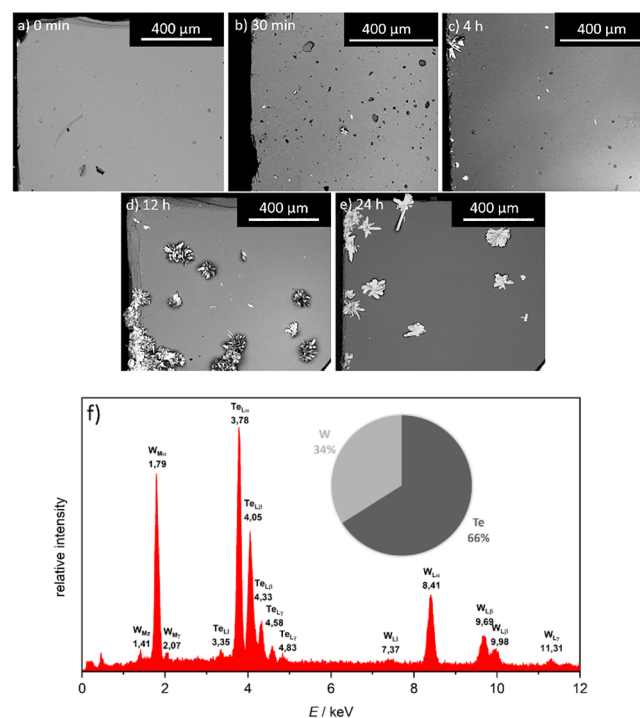


Figure 6. SEM image comparison of WTe₂ microstructures grown on YSZ (111) with different reaction times. $T_0 = 700$ °C, $\Delta T = 50$ K. (a) Almost no growth after heating period; (b) and (c) several crystal nuclei, no microsheets (d) crystals and agglomerates visible, smaller flakes in between (e) microstructures no longer visible; (f) EDX measurement (30 kV) at a bulky crystal agglomerate shows composition as WTe₂.

EDX of the larger agglomerates (Figure 6f) shows only W and Te as significant components in the material with a composition of 34 atom % W and 66 atom % Te, which is exactly at the expected composition of WTe₂. The described optimization process was monitored by constant SEM analysis of the substrates and the crystals on their surface. After successful optimization, we were able to synthesize promising structures shown in Figure 7. It is shown as grown structures with lateral dimensions of several microns that were visible on the YSZ (111) surfaces with a high aspect ratio of lateral dimensions/height.

Because of the depth of penetration of the method, the EDX analysis does not yield useful results for these structures, which indicates their thickness to be < 1 μm .

To determine the exact height of these structures, AFM as a complementary analyzing method has been applied.

Atomic Force Microscopy. The most promising structures were chosen, and their positions were marked to analyze them in AFM.

Several flakes were therefore measured in tapping mode as complete profile scans. Most of the sheets have heights around 20 nm, some are around 15 nm, and very few even under 10 nm. This equates to 14 (for 10 nm) or 29 (for 20 nm) structural layers of WTe₂ based on a van der Waals height of 7 Å each. The analysis of several substrates indicated that a higher transport time led to thinner nanosheets, which is consistent with the effect of a second temperature gradient in the ampule described above. However, it was hardly possible to control all the parameters that might contribute slightly to growth conditions, but that are finally influencing the height of

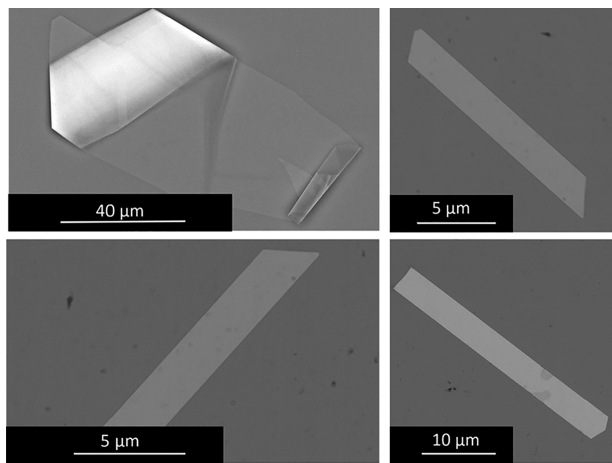


Figure 7. SEM images of several flakes as grown on the YSZ (111) surface after the optimization process.

sheets. Thus, the exact positioning of the substrate and the amount of starting material for each experiment on a microgram scale, respectively, were somewhat variable. To confirm this trend, more experiments with exact control over these additional parameters would have to be performed.

The small differences in height seen on top of some of the measured flakes (Figure 8a) and beside arise presumably from

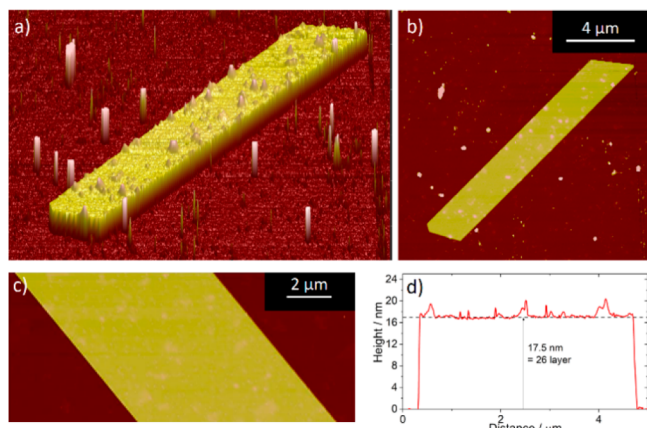


Figure 8. AFM of the WTe₂ crystals grown on YSZ (111) (a) and (b) 3D and 2D overview images of the measured flake, (c) position of the height profile measured in (d) height profile of the flake shows a height of 17.5 nm equating to 26 structural layers of WTe₂.

small contamination particles. They are only present in some of the structures and might be bromine species that deposited on the surface. Particles of bromine species could be transferred over from the transport agent when the quenching process is not fully done on T₂ first to ensure the transport agent fully solidifies on the source side instead of on the substrate.

AFM measurements clearly prove precipitation of WTe₂ by vapor transport with structures below 20 nm in height as grown while also reaching lateral dimensions of several microns. Thus, a bottom-up approach for direct synthesis of WTe₂ nanocrystals can be established.

Transmission Electron Microscopy and Electron Diffraction. Aberration-corrected high-resolution transmission electron microscopy (HR-TEM) and selected area

electron diffraction (SAED) were used to verify the orthorhombic crystal structure (space group Pmn2₁) of WTe₂ on the nano and atomic scale. To this end, the nanosheets were first transferred on a TEM copper mesh grid with lacey carbon support by gently wiping them off the surface of the YSZ(111) substrate. Using this method, we were able to transfer the structures without, e.g., any additional solvent. The WTe₂ flakes were therefore slightly squeezed and randomly oriented on the TEM grid forming a rather irregular morphology and presumably leading to not perfectly clear images. Small contamination particles as observed by AFM (Figure 8a) were not visible in the TEM.

An overview bright-field TEM image of a representative nanoflake is visible in Figure 9a, revealing its typical size and morphology. Figure 9b depicts the SAED pattern that was taken over the whole crystal shown in Figure 9a. The comparison with the theoretical diffraction pattern of 1T'-

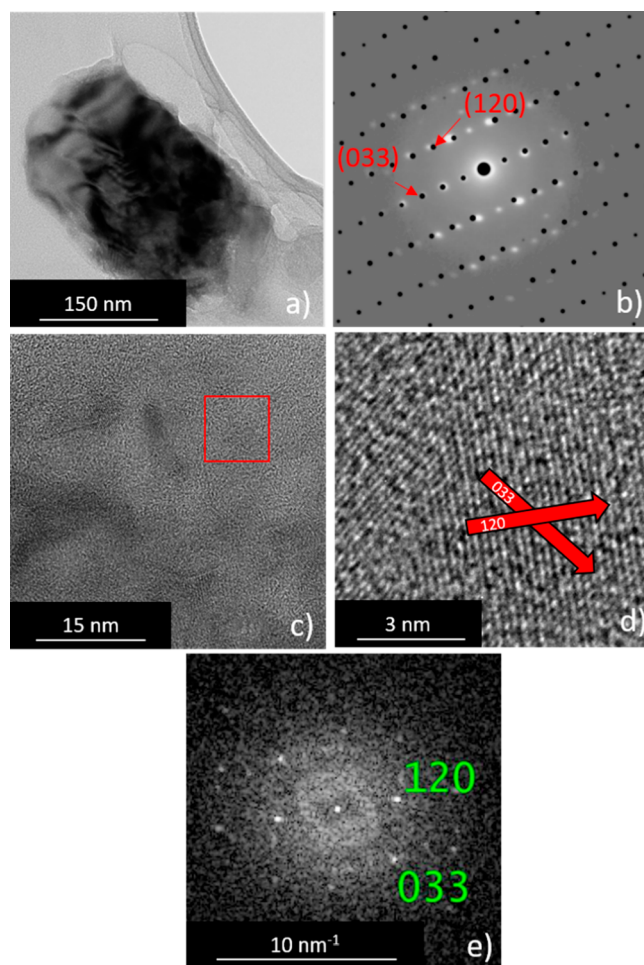


Figure 9. TEM investigation on WTe₂ nanoflakes. (a) Bright-field TEM overview image of a representative particle; (b) electron diffraction pattern of the whole particle shown in (a) superimposed by the calculated diffraction pattern (black dots) oriented in (-2 1 -1) zone axis direction of orthorhombic 1T'-WTe₂; (c) high resolution TEM image taken at the edge of the nanoflake mapping the atomic crystalline structure; (d) zoom-in of the region marked by a red square in (c) with lattice planes marked by red arrows and assigned to the Miller-indices of 1T'-WTe₂; (e) Fourier transform of (d) showing reflections corresponding to the indexed lattice planes.

WTe₂ (black dots) reveals a good match between the two with only small deviations at higher order reflections.

The HR-TEM image in Figure 9c shows the high crystallinity of the material, although the crystal structure is slightly disturbed at the edge of the nanoflake. For atomic imaging, only regions at the edge could be used, because they are only a few nanometers thin to be transparent for HR-TEM. A zoom-in (Figure 9d)) at the position indicated as a red square in Figure 9c displays the 120 and 033 lattice planes (red arrows) consistent with (−2 1 −1) zone axis orientation of the 1T'-WTe₂ crystal. This is supported by the Fourier transform of Figure 9d shown in Figure 9e confirming these assignments by single reflections of corresponding lattice plane *d*-spacings determined in real space.

The structure of 1T'-WTe₂ can therefore be confirmed for the material precipitated on the substrate by these HR-TEM and SAED experiments.

Polarized Raman Spectroscopy. The small laser spot size of $\sim 1 \mu\text{m}^2$ in the Raman microscope allowed us to measure polarized Raman spectra of single nanosheets. With such measurements, we could not only verify the material composition but also evaluate the crystallinity of the as-grown nanosheets.

In Figure 10a, the angle-averaged measurement of a single nanosheet is compared to the angle-averaged measurement of a 1T'-WTe₂ bulk crystal that was synthesized and evaluated by means of XRD beforehand. The comparison of the two Raman

signatures confirms the nanosheet to be WTe₂. The main signals found in the spectrum are at the same positions as in previous literature reports on WTe₂.^{41,42}

If incident light falls perpendicular to the *ab* plane of WTe₂ crystal and the Raman signal is collected in backscattered geometry, only A₁ and A₂ symmetry modes are active in Raman spectra of WTe₂ single crystal.⁴² Furthermore, A₁ and A₂ modes have different Raman tensors, leading to a different geometry of the polarization plane of the incident light and scattered (detected) light, at which these modes can be best detected.

A₁ modes should give the strongest response by $z(xx)\bar{z}$ and $z(yy)\bar{z}$ geometries and vanish by (xy) and (yx) orientations, whereas A₂ modes are most active at $z(yx)\bar{z}$ and $z(xy)\bar{z}$ geometry and vanish by (xx) and (yy) . In this notation, *z* and \bar{z} denote the direction of incident and scattered light, the first letter in parentheses is orientation of the polarization plane of the laser, whereas the second one denotes polarization of the detected light (controlled by the polarizer at the detector side). Thus, rotation of the laser polarization plane should lead to the situation when at certain angles only A₁ or only A₂ modes are active in the Raman spectrum of a well-ordered single crystal, whereas not well-ordered or polycrystalline sample will not show such a clear distinction.

Figure 10b shows polarized Raman spectra of WTe₂ nanosheets obtained at different angles of laser polarization plane with a step of 15°. Two panels correspond to the two perpendicular polarizations of the detected light. The spectra show a systematic variation of the peak intensities and allow the identification of two spectral patterns, which can be assigned to A₁ and A₂ modes by comparison to the literature data.^{41,42} A₁ modes (green curves in Figure 10b) are found at 80, 116, 132, 161, and 210 cm^{−1}.

Note that the peak intensities for $z(xx)\bar{z}$ and $z(yy)\bar{z}$ measurement geometries are different, in perfect agreement with the data reported by Kong et al. for a bulk single crystal of WTe₂. Rotation of the laser polarization plane by 90° results in an almost complete vanishing of the A₁ peaks and development of two bands at 89 and 110 cm^{−1} assigned to A₂ modes (red curves in Figure 10b). The strong polarization dependence and perfect distinction between A₁ and A₂ modes in corresponding orientations of polarization plane unambiguously prove very high single crystalline quality of WTe₂ nanosheets.

CONCLUSIONS

As a highlight, we succeeded in rational synthesis planning and experimental realization of bottom-up crystal growth of nanostructured WTe₂. The evaluation of optimum synthesis parameters achieved successful by modeling the phase diagrams and simulating vapor transport behavior in the system W/Te/Br. The current results complement earlier studies regarding a rational approach to the synthesis of nanolayers applying CalPhaD modeling and simulation,^{26,40} and provide the chance for bottom-up crystallization of nanostructured chalcogenides, too.

We determined the TeBr₂ to be functioning as a transport agent in the system and WBr₄ and Te₂ to be the species mainly active in the vapor transport. The temperature range between 650 and 750 °C proved to be the most suitable for crystallization via the gas phase. Therefore, we were able to successfully synthesize WTe₂ nanosheets by the bottom-up approach on the surface of YSZ(111) substrates with only few optimization steps to the synthesis. The optimum synthesis

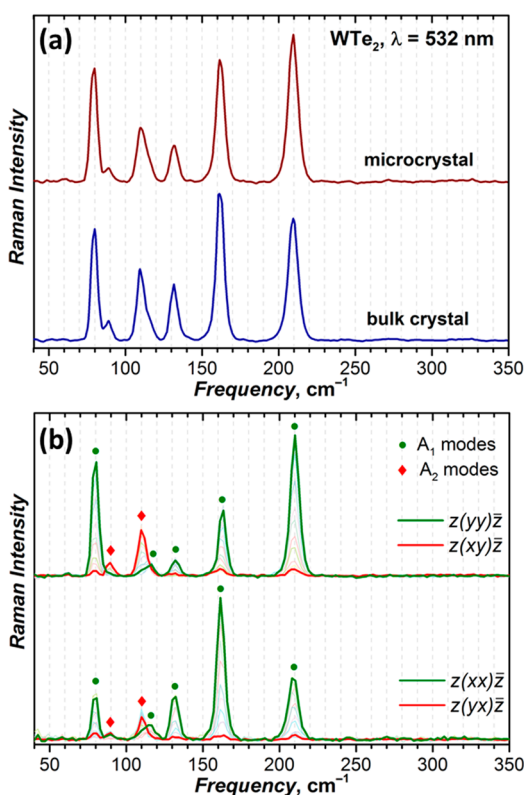


Figure 10. Polarized micro-Raman measurements of as-grown WTe₂ structures. (a) Measurement of a nanosheet compared to a 1T'-WTe₂ bulk crystal (averaged over all polarization angles), (b) angle dependent measurements of a single crystalline WTe₂ nanosheet on the YSZ (111) surface, polarization plane of the incident light is rotated with a step of 15°, two panels correspond to two orientations of the slit at the detector side.

parameters for achieving nanosheets emerged to be a transport time of 10 h with a temperature gradient of 50 K from $T_2 = 725^\circ\text{C}$ to $T_1 = 675^\circ\text{C}$. Scanning electron microscopy allowed us to identify promising, thin sheets that were further analyzed with atomic force microscopy and found to be 15–20 nm (20–30 layers of WTe₂) in height as grown. We are confident that with further research on the rational synthesis the tuning of thickness and size of the grown platelets on demand will become possible within the boundaries of the approach (e.g., most likely not down to a single monolayer). Polarized Raman spectroscopy and HR-TEM were applied to verify the structure and high crystallinity of the deposited structures. Comparison of the Raman spectra with those of bulk WTe₂ showed no significant changes from each other and from values reported in former research.^{41,42} HR-TEM and SAED proved the material to be WTe₂ with only minimal distortions visible in the SAED. Because of their ideal shape and thickness, the as-grown WTe₂ nanosheets prepared by our method are ideal candidates to use in further studies of, e.g., quantum transport properties and topological properties of few-layer WTe₂.

■ ASSOCIATED CONTENT

Supporting Information

The Supporting Information is available free of charge at <https://pubs.acs.org/doi/10.1021/acs.cgd.0c01004>.

Thermodynamic data used in the evaluation and modeling of the W/Te/Br system ([PDF](#))

■ AUTHOR INFORMATION

Corresponding Author

Felix Hansen — Leibniz Institute for Solid State and Materials Research Dresden, 01069 Dresden, Germany;  orcid.org/0000-0001-7387-9704; Email: f.hansen@ifw-dresden.de

Authors

Martin Wels — Brandenburg University of Technology Cottbus-Senftenberg, 01968 Senftenberg, Germany

Samuel Froeschke — Leibniz Institute for Solid State and Materials Research Dresden, 01069 Dresden, Germany

Alexey Popov — Leibniz Institute for Solid State and Materials Research Dresden, 01069 Dresden, Germany

Daniel Wolf — Leibniz Institute for Solid State and Materials Research Dresden, 01069 Dresden, Germany;  orcid.org/0000-0001-5000-8578

Bernd Büchner — Leibniz Institute for Solid State and Materials Research Dresden, 01069 Dresden, Germany; Technische Universität Dresden, 01069 Dresden, Germany

Peer Schmidt — Brandenburg University of Technology Cottbus-Senftenberg, 01968 Senftenberg, Germany;  orcid.org/0000-9618-4497

Silke Hampel — Leibniz Institute for Solid State and Materials Research Dresden, 01069 Dresden, Germany

Complete contact information is available at: <https://pubs.acs.org/10.1021/acs.cgd.0c01004>

Author Contributions

#F.H. and M.W. contributed equally.

Notes

The authors declare no competing financial interest.

■ ACKNOWLEDGMENTS

The authors gratefully thank Dr. Barbara Eichler, Sandra Schiemenz, and Robert Heider for the experimental help.

■ ABBREVIATIONS

CVT, chemical vapor transport; SEM, scanning electron microscopy; TEM, transmission electron microscopy; AFM, atomic force microscopy; SAED, selected area electron diffraction; HR-TEM, high-resolution transmission electron microscopy

■ REFERENCES

- (1) Novoselov, K. S.; Geim, A. K.; Morozov, S. V.; Jiang, D.; Zhang, Y.; Dubonos, S. V.; Grigorieva, I. V.; Firsov, A. A. Electric Field Effect in Atomically Thin Carbon Films. *Science* **2004**, *306* (5696), 666–669.
- (2) Mas-Balleste, R.; Gómez-Navarro, C.; Gómez-Herrero, J.; Zamora, F. 2D Materials: To Graphene and Beyond. *Nanoscale* **2011**, *3*, 20–30.
- (3) Wang, Z.; Gresch, D.; Soluyanov, A. A.; Xie, W.; Kushwaha, S.; Dai, X.; Troyer, M.; Cava, R. J.; Bernevig, B. A. MoTe2: A Type-II Weyl Topological Metal. *Phys. Rev. Lett.* **2016**, *117*, 1–5.
- (4) Gutiérrez, H. R.; Perea-López, N.; Elías, A. L.; Berkdemir, A.; Wang, B.; Lv, R.; López-Urías, F.; Crespi, V. H.; Terrones, H.; Terrones, M. Extraordinary Room-Temperature Photoluminescence in Triangular WS 2 Monolayers. *Nano Lett.* **2013**, *13*, 3447–3454.
- (5) Wang, X.; Gong, Y.; Shi, G.; Chow, W. L.; Keyshar, K.; Ye, G.; Vajtai, R.; Lou, J.; Liu, Z.; Ringe, E.; Tay, B. K.; Ajayan, P. M. Chemical Vapor Deposition Growth of Crystalline Monolayer MoSe2. *ACS Nano* **2014**, *8*, 5125–5131.
- (6) Lee, C. H.; Silva, E. C.; Calderin, L.; Nguyen, M. A. T.; Hollander, M. J.; Bersch, B.; Mallouk, T. E.; Robinson, J. A. Tungsten Ditelluride: A Layered Semimetal. *Sci. Rep.* **2015**, *5*, 1–8.
- (7) Zhu, Z.; Lin, X.; Liu, J.; Fauqué, B.; Tao, Q.; Yang, C.; Shi, Y.; Behnia, K. Quantum Oscillations, Thermoelectric Coefficients, and the Fermi Surface of Semimetallic WTe2. *Phys. Rev. Lett.* **2015**, *114*, 1–5.
- (8) Kang, D.; Zhou, Y.; Yi, W.; Yang, C.; Guo, J.; Shi, Y.; Zhang, S.; Wang, Z.; Zhang, C.; Jiang, S.; Li, A.; Yang, K.; Wu, Q.; Zhang, G.; Sun, L.; Zhao, Z. Superconductivity Emerging from a Suppressed Large Magnetoresistant State in Tungsten Ditelluride. *Nat. Commun.* **2015**, *6*, 6–11.
- (9) Ali, M. N.; Xiong, J.; Flynn, S.; Tao, J.; Gibson, Q. D.; Schoop, L. M.; Liang, T.; Haldolaarachchige, N.; Hirschberger, M.; Ong, N. P.; Cava, R. J. Large, Non-Saturating Magnetoresistance in WTe2. *Nature* **2014**, *514*, 205–208.
- (10) Cai, P. L.; Hu, J.; He, L. P.; Pan, J.; Hong, X. C.; Zhang, Z.; Zhang, J.; Wei, J.; Mao, Z. Q.; Li, S. Y. Drastic Pressure Effect on the Extremely Large Magnetoresistance in WTe2: Quantum Oscillation Study. *Phys. Rev. Lett.* **2015**, *115*, 1–5.
- (11) Peng, L.; Yuan, Y.; Li, G.; Yang, X.; Xian, J. J.; Yi, C. J.; Shi, Y. G.; Fu, Y. S. Observation of Topological States Residing at Step Edges of WTe2. *Nat. Commun.* **2017**, *8*, 1–7.
- (12) Ding, Y.; Zheng, W.; Jin, M.; Zhu, Y.; Zhu, R.; Lin, Z.; Huang, F. Raman Tensor of Layered WTe2. *J. Phys. Chem. C* **2020**, *124*, 16596–16603.
- (13) Lee, J.; Ye, F.; Wang, Z.; Yang, R.; Hu, J.; Mao, Z.; Wei, J.; Feng, P. X.-L. Single- and Few-Layer WTe₂ and Their Suspended Nanostructures: Raman Signatures and Nanomechanical Resonances. *Nanoscale* **2016**, *8*, 7854–7860.
- (14) Frenzel, A. J.; Homes, C. C.; Gibson, Q. D.; Shao, Y. M.; Post, K. W.; Charnukha, A.; Cava, R. J.; Basov, D. N. Anisotropic Electrodynamics of Type-II Weyl Semimetal Candidate WTe2. *Phys. Rev. B: Condens. Matter Mater. Phys.* **2017**, *95*, 2–6.
- (15) Zhang, Q.; Zhang, R.; Chen, J.; Shen, W.; An, C.; Hu, X.; Dong, M.; Liu, J.; Zhu, L. Remarkable Electronic and Optical

- Anisotropy of Layered 1T'-WTe₂ 2D Materials. *Beilstein J. Nanotechnol.* **2019**, *10*, 1745–1753.
- (16) Zhou, W.; Chen, J.; Gao, H.; Hu, T.; Ruan, S.; Stroppa, A.; Ren, W. Anomalous and Polarization-Sensitive Photoresponse of Td-WTe₂ from Visible to Infrared Light. *Adv. Mater.* **2019**, *31*, 1804629.
- (17) Brown, B. E. The Crystal Structures of WTe₂ and High-Temperature MoTe₂. *Acta Crystallogr.* **1966**, *20*, 268–274.
- (18) Mleczko, M. J.; Xu, R. L.; Okabe, K.; Kuo, H. H.; Fisher, I. R.; Wong, H. S. P.; Nishi, Y.; Pop, E. High Current Density and Low Thermal Conductivity of Atomically Thin Semimetallic WTe₂. *ACS Nano* **2016**, *10*, 7507–7514.
- (19) Zhou, J.; Liu, F.; Lin, J.; Huang, X.; Xia, J.; Zhang, B.; Zeng, Q.; Wang, H.; Zhu, C.; Niu, L.; Wang, X.; Fu, W.; Yu, P.; Chang, T. R.; Hsu, C. H.; Wu, D.; Jeng, H. T.; Huang, Y.; Lin, H.; Shen, Z.; Yang, C.; Lu, L.; Suenaga, K.; Zhou, W.; Pantelides, S. T.; Liu, G.; Liu, Z. Large-Area and High-Quality 2D Transition Metal Telluride. *Adv. Mater.* **2017**, *29*, DOI: 10.1002/adma.201603471.
- (20) Zhou, Y.; Jang, H.; Woods, J. M.; Xie, Y.; Kumaravadivel, P.; Pan, G. A.; Liu, J.; Liu, Y.; Cahill, D. G.; Cha, J. J. Direct Synthesis of Large-Scale WTe₂ Thin Films with Low Thermal Conductivity. *Adv. Funct. Mater.* **2017**, *27*. DOI: 10.1002/adfm.201605928.
- (21) Li, J.; Cheng, S.; Liu, Z.; Zhang, W.; Chang, H. Centimeter-Scale, Large-Area, Few-Layer 1T'-WTe₂ Films by Chemical Vapor Deposition and Its Long Term Stability in Ambient Condition. *J. Phys. Chem. C* **2018**, *122*, 7005–7012.
- (22) Zhou, J.; Lin, J.; Huang, X.; Zhou, Y.; Chen, Y.; Xia, J.; Wang, H.; Xie, Y.; Yu, H.; Lei, J.; Wu, D.; Liu, F.; Fu, Q.; Zeng, Q.; Hsu, C.-H.; Yang, C.; Lu, L.; Yu, T.; Shen, Z.; Lin, H.; Yakobson, B. I.; Liu, Q.; Suenaga, K.; Liu, G.; Liu, Z. A Library of Atomically Thin Metal Chalcogenides. *Nature* **2018**, *556*, 355–359.
- (23) Chen, K.; Chen, Z.; Wan, X.; Zheng, Z.; Xie, F.; Chen, W.; Gui, X.; Chen, H.; Xie, W.; Xu, J. A Simple Method for Synthesis of High-Quality Millimeter-Scale 1T' Transition-Metal Telluride and Near-Field Nanooptical Properties. *Adv. Mater.* **2017**, *29*, 1700704.
- (24) Lu, W.; Zhang, Y.; Zhu, Z.; Lai, J.; Zhao, C.; Liu, X.; Liu, J.; Sun, D. Thin Tungsten Telluride Layer Preparation by Thermal Annealing. *Nanotechnology* **2016**, *27*, DOI: 10.1088/0957-4484/27/41/414006.
- (25) Binnewies, M.; Glaum, R.; Schmidt, M.; Schmidt, P. *Chemical Vapor Transport Reactions*; De Gruyter: Berlin, Boston, 2016. DOI: 10.1515/9783110254655.
- (26) Grönke, M.; Schmidt, P.; Valldor, M.; Oswald, S.; Wolf, D.; Lubk, A.; Büchner, B.; Hampel, S. Chemical Vapor Growth and Delamination of α -RuCl₃ Nanosheets down to the Monolayer Limit. *Nanoscale* **2018**, *10*, 19014–19022.
- (27) Bale, C.W.; Belisle, E.; Chartrand, P.; Dechterov, S.A.; Eriksson, G.; Gheribi, A.E.; Hack, K.; Jung, I.-H.; Kang, Y.-B.; Melancon, J.; Pelton, A.D.; Petersen, S.; Robelin, C.; Sangster, J.; Spencer, P.; Van Ende, M.-A. FactSage Thermochemical Software and Databases, 2010 – 2016. *CALPHAD: Comput. Coupling Phase Diagrams Thermochem.* **2016**, *54*, 35–53.
- (28) Krabbes, G.; Bieger, K.; Sommer, H.; Söhnle, T.; Steiner, U. GMIN 5.1: Package TRAGMIN for Calculations of Thermodynamic Equilibrium. Dresden, 2014.
- (29) Obolonchik, V. A.; Nesterovskaja, L. M. Determination of WTe₂ Dissociation Pressure (in Russian). *Izv. Akad. Nauk SSSR, Neorg. Mater.* **1971**, No. 7, 498–499.
- (30) Callanan, J. E.; Hope, G. A.; Weir, R. D.; Westrum, E. F. Thermodynamic Properties of Tungsten Ditelluride (WTe₂) I. The Preparation and Lowtemperature Heat Capacity at Temperatures from 6 to 326 K. *J. Chem. Thermodyn.* **1992**, *24*, 627–638.
- (31) O'Hare, P. A. G.; Hope, G. A. Thermodynamic Properties of Tungsten II. Standard Molar Enthalpy of Formation at the Temperature 298. 15 K. *J. Chem. Thermodyn.* **1992**, *24* (6), 639–647.
- (32) Predel, B. Te-W (Tellurium-Tungsten). In *Pu-Re-Zn-Zr*; Madelung, O., Ed.; Springer-Verlag: Berlin/Heidelberg, 1998; pp 1–2. DOI: 10.1007/10551312_2825.
- (33) Philipp, F.; Schmidt, P.; Milke, E.; Binnewies, M.; Hoffmann, S. Synthesis of the Titanium Phosphide Telluride Ti₂PTe₂: A Thermochemical Approach. *J. Solid State Chem.* **2008**, *181*, 758–767.
- (34) Tschulik, K.; Ruck, M.; Binnewies, M.; Milke, E.; Hoffmann, S.; Schnelle, W.; Fokwa, B. P. T.; Gilleßen, M.; Schmidt, P. Chemistry and Physical Properties of the Phosphide Telluride Zr₂PTe₂. *Eur. Eur. J. Inorg. Chem.* **2009**, *2009* (21), 3102–3110.
- (35) Poddig, H.; Donath, T.; Gebauer, P.; Finzel, K.; Kohout, M.; Wu, Y.; Schmidt, P.; Doert, T. Rare Earth Metal Polytellurides RETe1.8 (RE = Gd, Tb, Dy) – Directed Synthesis, Crystal and Electronic Structures, and Bonding Features. *Z. Anorg. Allg. Chem.* **2018**, *644*, 1886–1896.
- (36) Binnewies, M.; Glaum, R.; Schmidt, M.; Schmidt, P. Chemical Vapor Transport Reactions - A Historical Review. *Z. Anorg. Allg. Chem.* **2013**, *639*, 219–229.
- (37) Binnewies, M.; Schmidt, M.; Schmidt, P. Chemical Vapor Transport Reactions – Arguments for Choosing a Suitable Transport Agent. *Z. Anorg. Allg. Chem.* **2017**, *643*, 1295–1311.
- (38) Binnewies, M.; Glaum, R.; Schmidt, M.; Schmidt, P. Crystal Growth Via the Gas Phase by Chemical Vapor Transport Reactions. *Handbook of Solid State Chemistry* **2017**, 351–374.
- (39) Brixner, L. H. Preparation and Properties of the Single Crystalline AB₂-Type Selenides and Tellurides of Niobium, Tantalum, Molybdenum and Tungsten. *J. Inorg. Nucl. Chem.* **1962**, *24*, 257–263.
- (40) Grönke, M.; Arrozi, U. S. F.; Bronkalla, N.; Schmidt, P.; Valldor, M.; Oswald, S.; Woodcock, T. G.; Eckert, V.; Hao, Q.; Plüschke, L.; Lederer, A.; Nielsch, K.; Büchner, B.; Kaskel, S.; Hampel, S. Layered α -TiCl₃: Microsheets on YSZ Substrates for Ethylene Polymerization with Enhanced Activity. *Chem. Mater.* **2019**, *31*, 5305–5313.
- (41) Cao, Y.; Sheremeteva, N.; Liang, L.; Yuan, H.; Zhong, T.; Meunier, V.; Pan, M. Anomalous Vibrational Modes in Few Layer WTe₂ Revealed by Polarized Raman Scattering and First-Principles Calculations. *2D Mater.* **2017**, *4*, DOI: 10.1088/2053-1583/aa7f5a.
- (42) Kong, W. D.; Wu, S. F.; Richard, P.; Lian, C. S.; Wang, J. T.; Yang, C. L.; Shi, Y. G.; Ding, H. Raman Scattering Investigation of Large Positive Magnetoresistance Material WTe₂. *Appl. Phys. Lett.* **2015**, *106*, 081906.